International Journal of Rock Mechanics & Mining Sciences 123 (2019) 104126

Contents lists available at ScienceDirect

International Journal of Rock Mechanics and Mining Sciences

journal homepage: http://www.elsevier.com/locate/ijrmms

Multibody failure criterion for the four-dimensional lattice spring model

Gao-Feng Zhao *, Zhi-Qiang Deng, Ben Zhang

State Key Laboratory of Hydraulic Engineering Simulation and Safety, School of Civil Engineering, Tianjin University, Tianjin, China

ARTICLE INFO

Keywords:
Lattice spring model
UCS/T ratio
Multi-body
Grain interlocking
Fabric stress tensor

ABSTRACT

Although lattice spring models (LSMs) have been increasingly applied in the study of rock fracturing and rock failure, it is still difficult to accurately reproduce high ratios of the uniaxial compressive strength to the tensile strength of rock materials. In this work, a feasible solution is developed for the four-dimensional lattice spring model (4D-LSM) that overcomes this shortcoming by incorporating a multibody failure criterion. The stress tensor of a spring bond is determined by the local deformation state between this bond and its neighboring spring bonds, which is further used to judge its failure state using a stress-based strength model. Then, a cohesive zone model is introduced to describe the postfailure stage of the spring bond. The performance of the proposed solution in reproducing the high ratio of the uniaxial compressive strength to the tensile strength of rock materials is demonstrated via numerical tests. Enriched by the multibody failure criterion, 4D-LSM is demonstrated to solve a broader range of practical problems that involve rock failure.

1. Introduction

The ratio of the uniaxial compressive strength to the uniaxial tensile strength (UCS/T ratio) of a material is considered one of the most important indicators of its mechanical properties. For example, a unified strength criterion[1] was developed based on the UCS/T ratio for many types of materials, including rocks, ceramics, and metals. For continuum-based numerical methods, such as the finite element method (FEM), it is straightforward to reproduce the designed UCS/T ratio since it is an input of the constitutive model. However, for discontinuum-based numerical methods, such as the discrete element model (DEM) and the lattice spring model (LSM), it is typically difficult to reproduce the high UCS/T ratio that is observed in rock materials. For DEM, insufficient grain interlocking and rotational resistance of circular/spherical particles cause the low UCS/T ratio.[2–6] To tackle this problem, many solutions have been developed. These methods can be divided into geometry-based approaches and constitutive-model-based approaches.

The most representative geometry-based approach is the clumped particle scheme that was developed by Cho et al.[4] for characterizing mineral crystals inside rocks. The internal particle bonding strength of a clumped particle has a higher strength compared to the particles along the boundary of the clumped particle. By modifying the mechanical parameters of the clumped particle model, the UCS/T ratio of DEM has been successfully increased to 14.29. Another typical approach is to use polygonal particles to consider the grain interlocking. For example, Kazerani and Zhao[5] used polygonal particles to characterize the microstructures of rock materials. Uniaxial compression and Brazilian disk tests were used to test the polygonal particle model, according to which the UCS/T ratio that was obtained by the polygonal particle model was consistent with the corresponding experimental results. Directly mapping the realistic rock microstructure is another a possible solution. For example, Zhao et al.[6] successfully reproduced the high UCS/T ratio (12.35) by using the distinct lattice spring model (DLSM) to construct a computational model that was based on a microscope polarized digital image of a fine-grained rock. These geometry-based approaches are easy to understand and to implement. However, there are several shortcomings. For example, Ding and Zhang[7] found that for DEM, the UCS/T ratio could only increase slightly in a small range if some spherical particles were replaced by polyhedral block particles, and it is necessary to introduce more complex particles. Moreover, the use of particles with complex shapes might lead to heterogeneity, anisotropy and scale effects, which further complicate the correlation between the micro parameters of the discrete model to the corresponding experimentally measured mechanical parameters, such as the elastic modulus, the Poisson's ratio, the friction angle, and the cohesion.[8] Furthermore, the pre-processing that is involved in these approaches is typically cumbersome and the corresponding computational cost is high. Therefore, reports on the use of approaches of this type in practical applications are rare in the literature.

* Corresponding author.
E-mail address: gaofeng.zhao@tju.edu.cn (G.-F. Zhao).

https://doi.org/10.1016/j.ijrmms.2019.104126
Received 24 July 2019; Received in revised form 29 August 2019; Accepted 26 September 2019
Available online 3 October 2019
1365-1609/© 2019 Elsevier Ltd. All rights reserved.

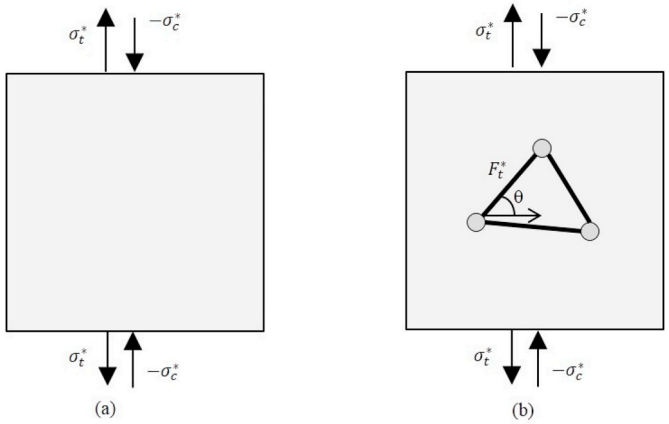

Fig. 1. Mechanical analysis models of a material under uniaxial tension and uniaxial compression: (a) The continuum-based approach and (b) the discontinuum-based approach.

In addition to modifying the geometries of the particles, a high UCS/T ratio can also be realized by modifying the connections between particles, which can be regarded as another type of geometrical approach. For example, Schöpfer et al.[9] found that the UCS/T ratio was related to the number of bonds between particles in DEM. A high UCS/T ratio can be obtained by removing the bonds between some of the particles, which can simulate the micro-crack structure inside the rock. Particles without bonds in the model cannot withstand tensile and shear stresses; however, they can withstand compressive stress, thereby increasing the UCS/T ratio at the macro level. Via this approach, Ding and Zhang[7] doubled the UCS/T ratio of a particle DEM model that was built by PFC3D but still failed to reach the experimentally observed value. Researchers have also attempted to increase the interlocking between particles by increasing the number of bonds between particles in DEM.[3,10,11] This method can increase the UCT/S ratio to more than 20.[3,12] However, this approach causes the bonded DEM to fail to reproduce the correct elastic boundary value problem prior to failure.[13]

The constitutive-model-based approach is more flexible because it does not require pre-processing of a complex computational model for considering the internal microstructure of rock. For example, Potyondy[2] modified the contact model between particles in PFC to reduce the rotation effect of the bonds between particles by eliminating the normal and tangential stresses that are caused by the bending moment or torque, thereby delaying the break of the bonds, which successfully reproduced the UCS/T ratio of diorite. Ding and Zhang[14] proposed a new contact model that considers the effects of the moment of the normal and tangential stresses on contact failure. Their results demonstrated that the moment, cohesion and tensile strength were three key input parameters that affect the model's UCS/T ratio. Fakhimi[15] proposed a constitutive model of micro-overlapping discs, in which slight overlaps of the discs that constitute the computational model are permitted, and he reproduced an UCS/T ratio of up to 9.95 using sufficiently small particles. Wu and Xu[16] developed a plane contact model in PFC for addressing the low UCS/T ratio of DEM. In their model, the interaction between particles was represented as a contact between two imaginary surfaces, which were divided into several elements. It was more convenient to obtain realistic UCS/T ratios of rock materials by modifying the constitutive model. Nevertheless, additional parameters and operations were typically required in these modified constitutive models, which further complicates the computations and the parameter calibration process. Moreover, DEM with these modified constitutive models might produce unstable numerical results in the postfailure stage of rock.

For LSMs, recent studies have focused on overcoming the Poisson's ratio limitation using various models, such as DLSM[17] and the four-dimensional lattice spring model (4D-LSM),[18] among other models.[19,20] Although LSMs have many advantages and are convenient for handling the crack propagation of brittle materials,[19–22] the models are unable to reproduce the high UCS/T ratios of rock materials.[23] Due to the difference in the discretization strategies between LSM and DEM, these new constitutive models for DEM cannot be directly implemented into LSMs such as the newly developed 4D-LSM. The objective of this study is to develop a more general and straightforward solution for the low UCS/T ratio problem of 4D-LSM. We start from a simple macroscopic mechanical analysis of the reason for the low UCS/T ratio of the discrete model (DEM and LSM). On this basis, a multibody failure criterion for the spring bond is developed for solving the low UCS/T ratio problem. Following this, the performance of this scheme is evaluated via numerical simulation of uniaxial compressive and tensile tests. Finally, typical problems that are related to rock failure are analyzed and compared with the corresponding experiential observations to further evaluate the applicability of the proposed solution.

2. Mechanical analysis of the low UCS/T ratio problem

A classical explanation of the low UCS/T ratio problem of DEM is its insufficient representation of grain interlocking in rock materials. Since this is a microscopic interpretation, solutions that are based on this mechanism are limited in terms of generalization as follows: The UCS/T ratio cannot be a direct input parameter but should be indirectly controlled by other factors such as the particle geometry and additional constitutive parameters with micromechanical meanings. Here, we use a cubic unit model to macroscopically analyze the mechanical response of rock under uniaxial tension and uniaxial compression (see Fig. 1). For the continuum-based model (see Fig. 1a), assuming we are following the basic definitions of elastic mechanics, the compressive stress is negative and the tension stress is positive. In the tension and compression state of the unit, the ultimate stresses in the loading and lateral directions can be expressed as $(\sigma_t^*, 0)$ and $(-\sigma_c^*, 0)$, respectively, where the tensile strength σ_t^* and the compressive strength σ_c^* are independent material parameters. Therefore, the UCS/T ratio can be an input parameter for these continuum-based models. As shown in Fig. 1b, if we represent the material unit using a discontinuum-based (discrete) model that only considers the central pair interaction, the interaction force between two particles can be expressed as

$$F = ku \tag{1}$$

where F is the interaction force between two particles, k is the spring stiffness, and u is the spring deformation. Under uniaxial tension or uniaxial compression, the unit body is in a simple strain state. For a specified axial stress, the force of the spring bond can be expressed as

$$F = k(\varepsilon_x l \quad \varepsilon_y l) \cdot (\cos\theta \quad \sin\theta)^T = \frac{\sigma l k}{E}(\sin\theta - \nu\cos\theta) \tag{2}$$

where E is the elastic modulus of the material, ν is the Poisson's ratio of the unit, θ is the angle between the bond and the horizontal direction, σ is the axial stress of the unit, and l is the length of the bond. We denote the tensile strength of the bond as F_t^* and assume that macroscopic failure of the material unit will occur only if at least one spring bond satisfies the bond's failure criterion. In addition, we assume that the spring bond is randomly distributed and the bond orientation can be any value from 0 to 180°. Under this assumption and according to Eq. (2), under tension loading, the most critical spring bond angle is $\theta = 90°$. Then, the relationship between the macroscopic tensile strength and the spring tensile strength can be expressed as

$$\sigma_t^* = \frac{F_t^* E}{lk} \tag{3}$$

Since the tensile strength of the spring bond can be related to the

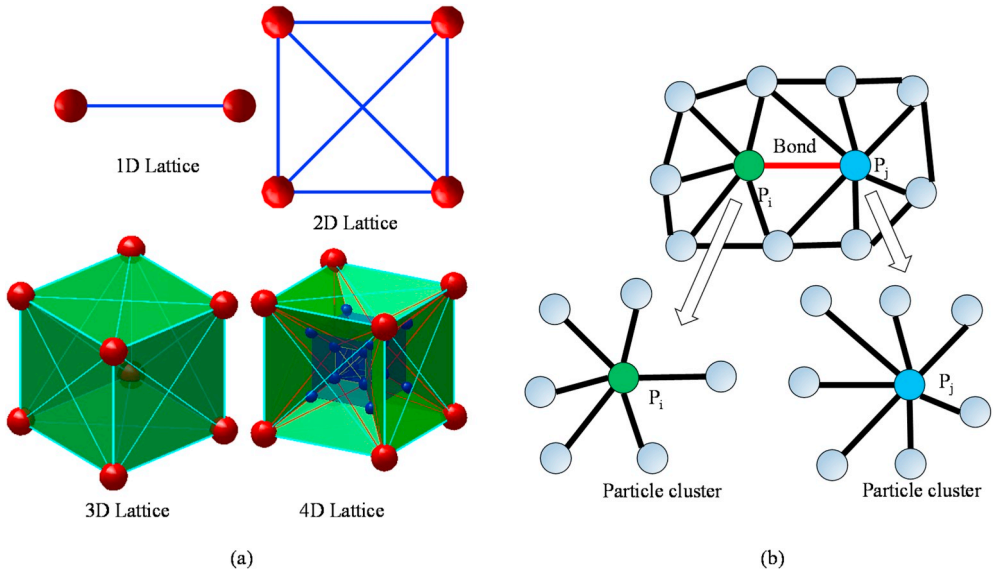

Fig. 2. Lattice structure of 4D-LSM and the calculation of the bond stress tensor. (a) Illustrations of 1D to 4D lattices and (b) particle clusters for calculating the bond stress tensor.

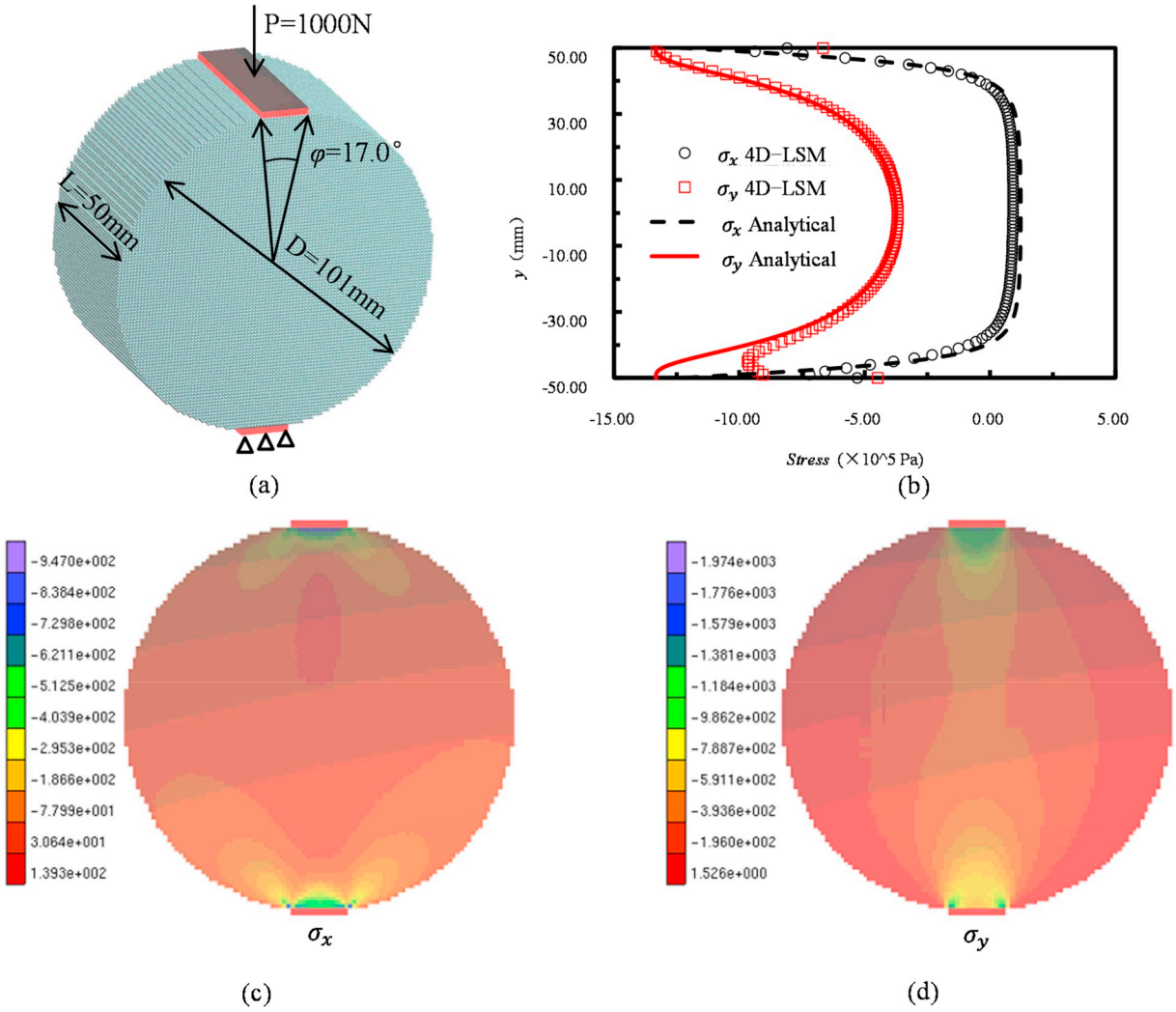

Fig. 3. Brazilian disc numerical test by using 4D-LSM. (a) The computational model and boundary conditions, (b) analytical results from Hondros[25] and 4D−LSM, (c) a σ_x stress contour, and (d) a σ_y stress contour.

Table 1
Mechanical parameters of numerical models.

Numerical example	Elastic Modulus (MPa)	Poisson's ratio	Density (kg/m^3)	Tension strength (MPa)	Frication angle	Cohesion (MPa)	dRatio
Brazilian test	25800	0.23	2700	8.8	53	21	0.3
Uniaxial compression/tension test	25800	0.23	2700	8.8	53	21	0.3/0.5/0.7/0.9
Failure of specimens containing a single round hole	98000	0.21	2601	15.5	40	18	0.3
Slope failure	49900	0.25	1700	0.05	32	0.4	0.3

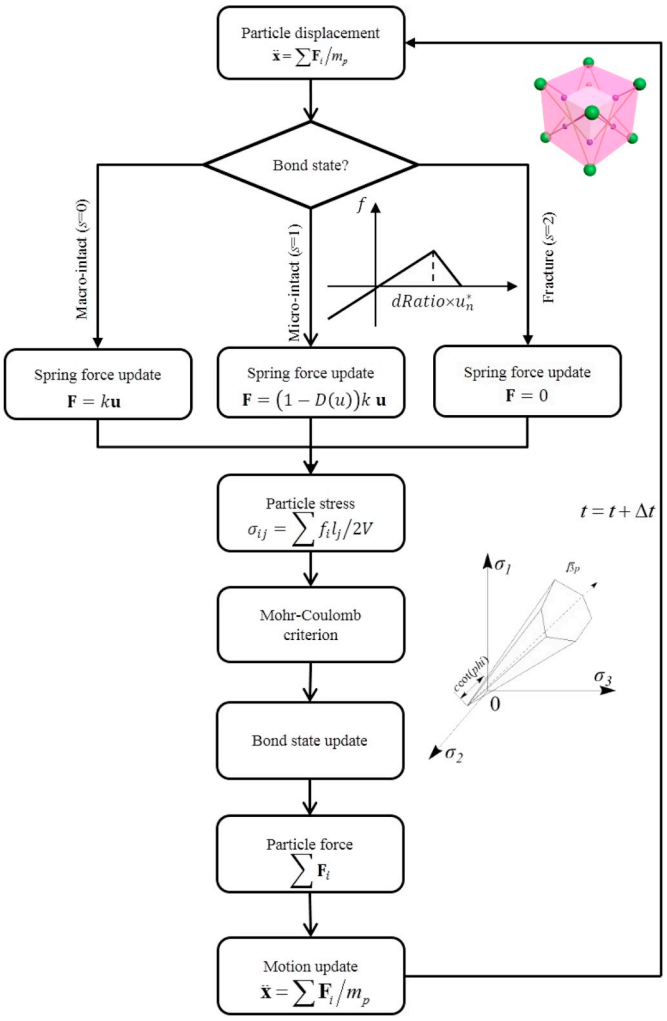

Fig. 4. Flow diagram of the 4D−LSM calculation procedure with the multibody failure criterion.

ultimate tensile deformation as $u^* = \frac{F_t^*}{k}$, the ultimate tensional deformation of the spring bond can be further expressed as

$$u^* = \frac{\sigma_t^* l}{E} \tag{4}$$

Eq. (4) provide a basis for the selection of the tensile parameter in DLSM. Zhao[22] has demonstrated the applicability of this formula. The relationship between the spring deformation between two particles and the stress intensity factor is found to be correlated by Jiang et al.,[21] which further supports that the simple ultimate deformation rule for a spring bond can handle cracking. Based on the same assumption and a similar principle, the uniaxial compressive strength of the material unit can be further expressed as

$$\sigma_c^* = -\frac{F_t^* E}{vlk} \tag{5}$$

According to this equation, the uniaxial tensile and compressive strengths of the discrete model are correlated. Substituting Eq. (3) into Eq. (5), UCS/T ratio of the unit can be expressed as

$$\left|\frac{\sigma_c}{\sigma_t}\right| = \frac{1}{v} \tag{6}$$

For rock materials, the Poisson's ratio is approximately 0.2–0.33. Then, the UCS/T ratio that is predicted by Eq. (6) is between 3 and 5, which is similar to the range that is predicted by DEM and LSM without special treatment. The tensile strength criterion $F \geq F_t^*$ for the spring bond is controlled by the bond's deformation, which is relevant to the strain-based strength criterion. That is a historical problem of material strength theory. According to Yu,[24] the strain-based strength model was withdrawn from history due to the inconsistency between its predicted results and experimental results. From this perspective, researchers who are working on discrete models are unconsciously reversing this conclusion on the microscopic level. For a discrete model, from a macroscopic perspective, the strain-controlled strength criterion is inevitably implicitly applied if the tensile failure of the spring bond is considered independently, which could lead to a low UCS/T ratio. If we can apply the stress-based strength criterion to a discrete model, the UCS/T ratio problem might be resolved. When we revisit the elastic Hooke's law in three-dimensional space, we find that the stress-based strength model considers the coupling of the deformations (strains) along with three directions simultaneously. For example, we consider the principle stress space for axial stress $\sigma_1 = \frac{E}{(1+\nu)(1-2\nu)}((1-\nu)\varepsilon_1 + \nu(\varepsilon_2 + \varepsilon_3))$, in which σ_1 is determined from the strains in multiple directions. Therefore, if the failure state of a spring bond can be determined from its deformation and from the deformations of its neighbors, it might be able to fully reproduce the stress-based strength model and to solve the UCS/T ratio problem.

2.1. Multibody failure criterion of a spring bond

In this section, a multibody failure criterion of a spring bond is introduced for solving the low UCS/T ratio problem of 4D-LSM. This approach is also applicable to other discrete models such as DLSM and DEM. The most distinct feature of 4D-LSM is its lattice structure, which was defined in a 4D space. In Fig. 2a, illustrations of the 1D to 4D lattices are presented to facilitate understanding. A more detailed explanation and a mathematical proof of 4D-LSM can be found in the original reference.19 To derive the equation for obtaining the stress tensor of the spring bond, the computational model that is used in 4D-LSM is represented as a network, as illustrated in Fig. 2b. A particle with its adjacent particles constitute a particle cluster and the stress state of this particle can be expressed in terms of the deformation states of these spring bonds around the particle as

$$\sigma_{ij}^I = \frac{1}{2V^I} \sum_{J=0}^{N} f_i^{IJ} n_j^{IJ} l_0^{IJ} \tag{7}$$

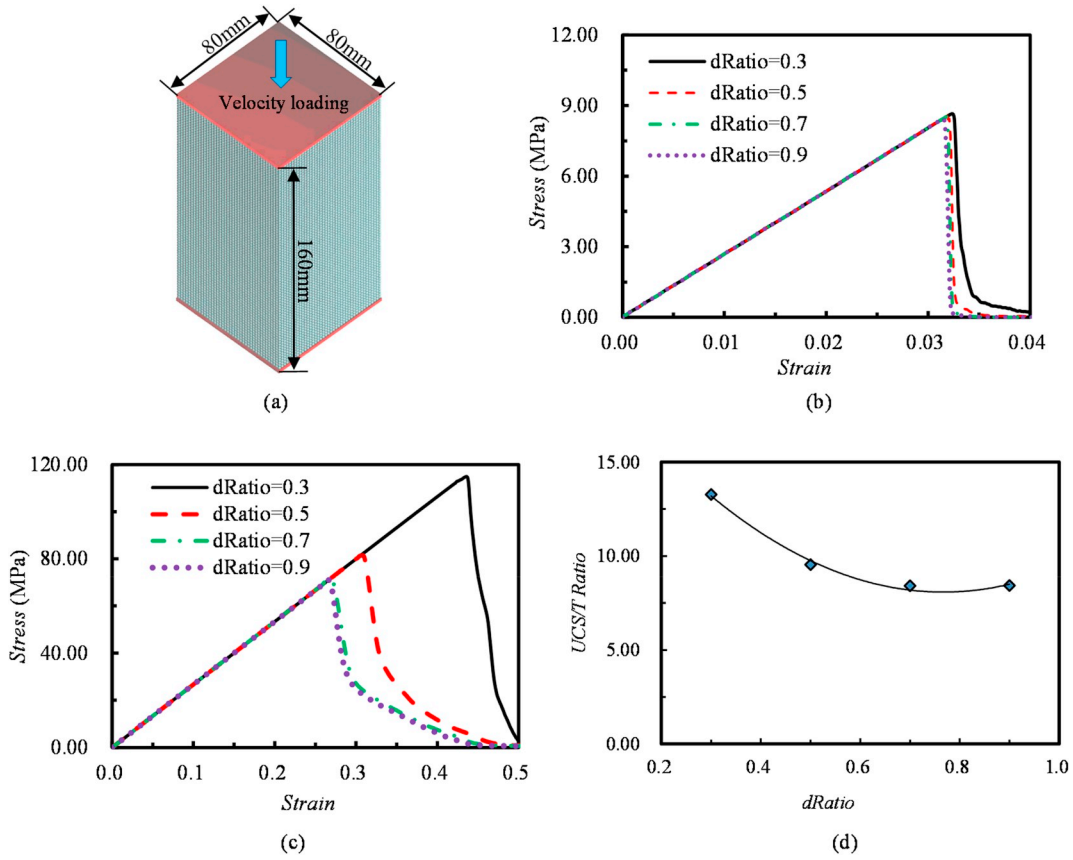

Fig. 5. Numerical modelling of uniaxial compression and tension tests using 4D-LSM. (a) The computational model and boundary conditions, (b) the uniaxial tensional strength as a function of *dRatio*, (c) the uniaxial compressive strength as a function of *dRatio*, and (d) the UCS/T ratio versus *dRatio*.

where σ_{ij}^{I} is the stress tensor of particle I, V^{I} is the represented volume of the particle, f_i^{IJ} is the interaction force component between particle I and its neighbors, n_j^{IJ} is the normal vector component between particle I and its neighbors, and l_0^{IJ} is the initial spring length between particle I and its neighbors. Eq. (7) can be proved via hyperelasticity analysis, which will be further explained in Section 2.3. The stress state of a spring bond is expressed as

$$\boldsymbol{\sigma}_{ij}^{bond} = \frac{\boldsymbol{\sigma}_i + \boldsymbol{\sigma}_j}{2} \tag{8}$$

Then, the failure of each spring bond is determined using a macroscopic stress-based strength model, such as the modified Mohr-Coulomb criterion:

$$f\left(\boldsymbol{\sigma}_{ij}^{bond}\right) = f\left(\sigma_1^{bond}, \sigma_3^{bond}\right) = \begin{cases} (1-\sin\phi)\sigma_1^{bond} - (1-\cos\phi)\sigma_3^{bond} - 2c\cos(\phi) \geq 0 \\ \\ \sigma_1^{bond} - \sigma_t^{*} \geq 0 \end{cases} \tag{9}$$

where σ_1^{bond} and σ_3^{bond} are the first and third principal stresses, respectively, of the stress tensor of the corresponding spring bond; ϕ is the internal friction angle; c is the cohesion; and σ_t^{*} is the tensile strength. The fabric stress tensor of a spring bond is determined from the current spring bond forces of its linked particles, which are further determined by the bond deformations of the springs of these particles. The failure state of a spring bond is determined from the deformation states of a group of connected spring bonds; therefore, we call this approach the multibody failure criterion of the spring bond. The applicability of the fiber stress tensor that was obtained via Eq. (7) to the representation of the actual stress state of the lattice model is essential for this approach, which will be proved in the following section.

2.2. Proof of the fiber stress formula

Newly developed discrete model 4D-LSM overcomes the Poisson's ratio limitation in the classical LSM by introducing four-dimensional spatial interactions. This model is similar to traditional DEM and molecular dynamics (MD) in various respects. For example, they all use Newton's second law to solve the corresponding motion equations. The main differences are that each particle in 4D-LSM includes not only three degrees of freedom but also considers a fourth spatial degree of freedom, and the connections between particles in 4D-LSM correspond to interactions in a four-dimensional space (see Fig. 2a). The construction of 4D-LSM is based on the concept of a parallel world, in which the four-dimensional connection is generated by the interconnection between the original three-dimensional model and the corresponding model in a parallel world. The first step is to set up the 3D lattice model, which is composed of 3D particles and springs that connect them. The second step is to offset this 3D model along the 4th dimension by one lattice length to form a parallel model. The parallel model is invisible in the original 3D space. The last step is to connect these two models through 4D interactions.[12] In 4D-LSM, the stiffness (k^{3D}) of these springs is the same when interacting in three-dimensional space. There are three types of springs in the four-dimensional space, which are represented by stiffnesses k_α, k_β and k_γ. To reproduce the isotropic elastic mechanical response, the four-dimensional spring stiffnesses and the three-dimensional spring stiffness should be related as follows:

$$k_\alpha = k_\beta = \frac{4}{3}k_\gamma = \lambda^{4D}k^{3D} \tag{10}$$

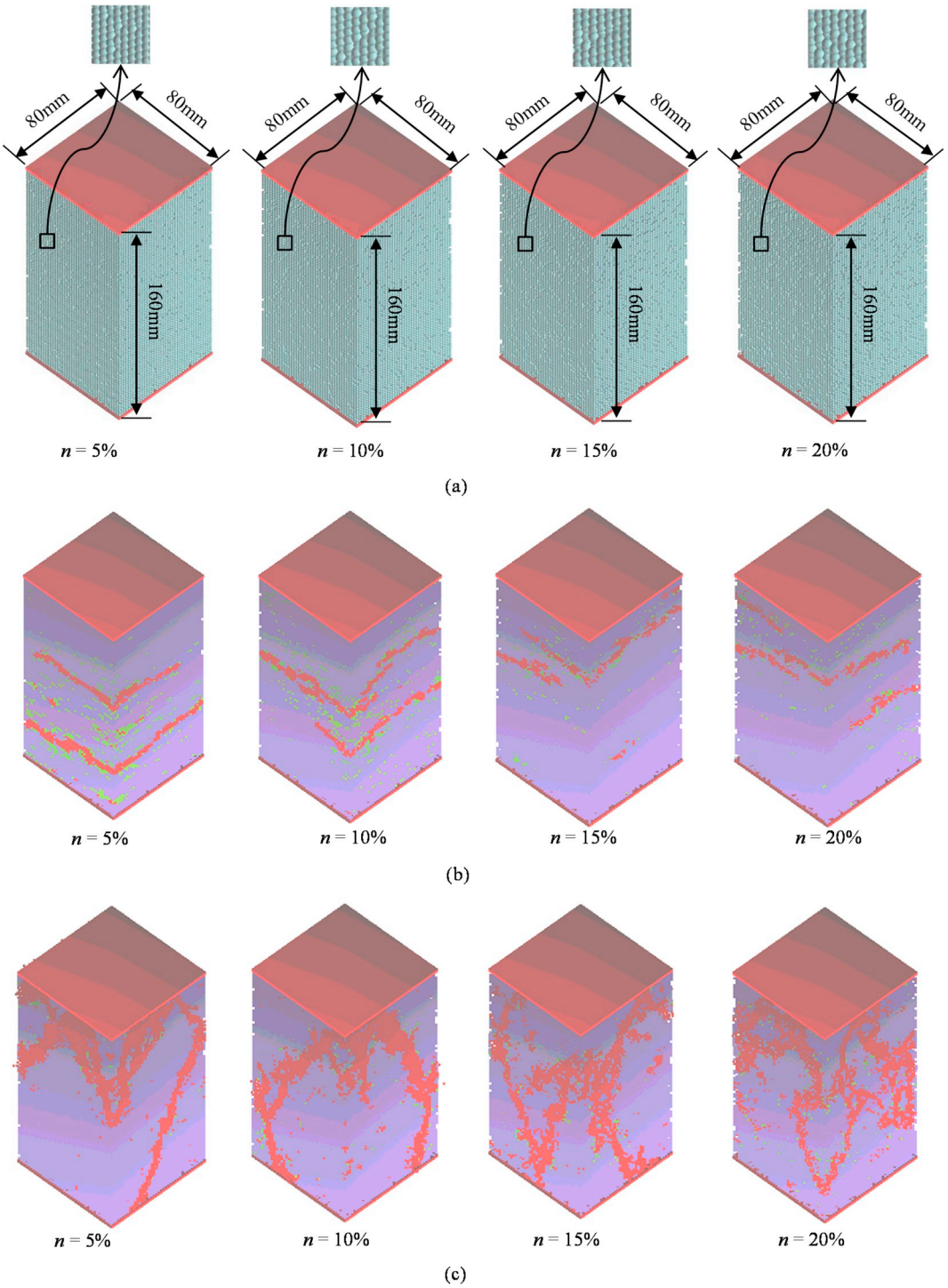

Fig. 6. Numerical modelling of compressive and tension failures of a porous solid using 4D-LSM.

where k_α, k_β and k_γ are the four-dimensional spring stiffnesses and λ^{4D} is a four-dimensional stiffness ratio, which can be determined from the Poisson's ratio. In the elastic stage, the interaction between two particles is expressed as

$$\mathbf{F}_{ij} = k u_n \mathbf{n}_{ij} \tag{11}$$

where $\mathbf{F}_{ij}$ is the four-dimensional force from particle i to particle j; $\mathbf{n}_{ij}$ is the four-dimensional normal vector from particle i to particle j; k is the stiffness of the corresponding spring, where the value ($k^{3D}k_\alpha, k_\beta$ or k_γ) of k is determined by the type of spring; and u_n is the deformation of the four-dimensional spring, which is characterized by the Euler length as

$$u_n = \left|\mathbf{x}_j - \mathbf{x}_i\right| - \left|\mathbf{x}_j^0 - \mathbf{x}_i^0\right| \tag{12}$$

where $\mathbf{x}$ is the current position of the particle, $\mathbf{x}^0$ is the initial position of the particle, and $|\bullet|$ denotes the Euler distance between the two particles' positions. Although the four-dimensional space is difficult to understand, the calculation only differs in terms of the number of components of the vector or the tensor, and all rules and definitions remain the same as in three-dimensional space. The formula for calculating the fiber stresses, which is presented in Eq. (7), has a similar form

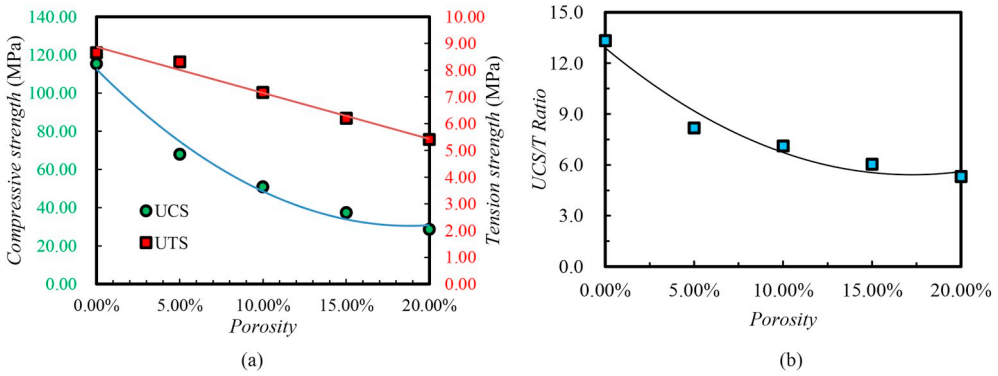

Fig. 7. Numerical prediction of the effects of porosity on the compressive and tensile strengths using 4D-LSM with the multibody failure criterion.

to those that are used in DEM. The only difference is the involvement of fourth dimension in the calculation. Since 4D-LSM was defined in four-dimensional space, its stress tensor is 4D. However, since the plane stress assumption is adopted in 4D-LSM along the fourth dimension (hyper membrane), the stress tensor that is calculated via Eq. (7) can be further simplified as the classical three-dimensional stress tensor, namely, the components that contain the indices for the fourth dimension are zero. Now, we will further evaluate the applicability of Eq. (7) for 4D-LSM via hyperelasticity analysis. Consider a particle cloud in 4D-LSM that contains a series of spring bonds and assume that a simple deformation field ε_{ij} is applied to it. The normal deformation of a spring bond can be expressed as

$$u_n = \varepsilon_{ij} n_j n_i l_0 \tag{13}$$

If the reprehensive volume of the particle is V, the strain energy density of the particle can be expressed as

$$\Omega = \frac{1}{2}\frac{1}{V}\sum\frac{1}{2}ku_n^2 = \frac{1}{4V}\sum ku_n^2 \tag{14}$$

According to the hyperelasticity analysis, the corresponding stress of the particle can be expressed as

$$\sigma_{ij} = \frac{\partial\Omega}{\partial\varepsilon_{ij}} = \frac{1}{2V}\sum(k\varepsilon_{ik}n_k l_0)(n_j l_0) = \frac{1}{2V}\sum f_i n_j l_0 \tag{15}$$

Eq. (7) is the general form of Eq. (15). In contrast to DEM, the particle stress in 4D-LSM is determined at each particle rather than over a measurement sphere that contains multiple particles. In this work, we will verify Eq. (15) by calculating the splitting stress of the classical Brazilian disc test. Assuming the disk is homogeneous and isotropic, the theoretical formulas of the compressive stress and tensile stress distributions within the linear elastic range are[25,26]

$$\sigma_y = -\frac{2P}{\pi R\phi L}\left[\frac{\left(1-\frac{r^2}{R^2}\right)\sin\phi}{1-\left(2\frac{r^2}{R^2}\right)\cos\phi+\frac{r^4}{R^4}} + \arctan\left(\frac{1+\frac{r^2}{R^2}}{1-\frac{r^2}{R^2}}\tan\frac{\phi}{2}\right)\right] \tag{16}$$

$$\sigma_x = -\frac{2P}{\pi R\phi L}\left[\frac{\left(1-\frac{r^2}{R^2}\right)\sin\phi}{1-\left(2\frac{r^2}{R^2}\right)\cos\phi+\frac{r^4}{R^4}} - \arctan\left(\frac{1+\frac{r^2}{R^2}}{1-\frac{r^2}{R^2}}\tan\frac{\phi}{2}\right)\right] \tag{17}$$

where σ_y is the stress along the vertical direction; σ_x is the stress along the horizontal direction; P is the applied external load; R is the radius of the disk; L is the thickness of the disk; ϕ is the arc angle that is applied by the external load; and r is the radial distance from the center of the disk, where $r = 0$ at the center of the disk (see Fig. 3a). The mechanical parameters of the disk are listed in Table 1. The vertical and horizontal stresses of the particles along the loading direction in the numerical modeling using 4D-LSM with Eq. (7) are extracted and compared with the theoretical solutions of Eqs. (16) and (17). The results are presented in Fig. 3b. The simulated values of σ_x and σ_y are consistent with the theoretical values, except in the bottom region, where the theoretical values of σ_y differ slightly from the numerically predicted values; hence, the calculated fiber stress can be used to represent the stress state of the disk. In contrast to the Cauchy stress tensor, Eq. (7) is independent of the rigid-body rotation and has an intrinsic size; therefore, it is suitable for failure analysis that involves large deformations.

2.3. Postfailure stage of a spring bond

In this work, the pre-failure stage of a spring bond is characterized by a linear elastic model and the postfailure stage is described by a cohesive zone model, which is expressed as the following damage model:

$$f = \begin{cases} ku_n & , \quad f\left(\sigma_{ij}^{bond}\right) < 0 \\ (1-D)ku_n & , \quad f\left(\sigma_{ij}^{bond}\right) \geq 0 \end{cases} \tag{18}$$

where D represents the amount of damage to the spring bond and its initial value is $D = 0$. There are four types of springs in 4D-LSM, which are described by stiffnesses k^{3D}, k_α, k_β and k_γ. In this work, we assume the damage of the four-dimensional spring stiffness k_α is constant and equal to 0. k_β and k_γ are related to the damage of the corresponding three-dimensional spring bond that is associated with them. This assumption can be expressed as

$$D^{AA'} \equiv 0, D^{AB} = D^{A'B'} = D^{A'B'} = D^{A'B'} \tag{19}$$

where A and B represent two particles in the original three-dimensional space and A' and B' represent two mapped particles in the corresponding parallel space. By defining the damage function of the spring bond in the original three-dimensional space, the behaviors of all spring bonds after the strength criterion has been satisfied can be determined. In this work, a linear softening model is adopted, which is expressed as

$$D(u_{3D}) = \begin{cases} 1 - \dfrac{u_{3D}^* - dRatio\cdot u_{3D}}{(1-dRatio)u_{3D}^*} & , \quad u_{3D} \leq u_{3D}^*/dRatio \\ 1 & , \quad u_{3D} > u_{3D}^*/dRatio \end{cases} \tag{20}$$

where $dRatio$ is the ratio of the deformation that corresponds to the peak point to the final deformation, and u_{3D}^* is the peak deformation, which is expressed as the spring elongation $u_{3D}(t^*)$ when the spring satisfies the multibody failure criterion. Since the elongation of the spring may be negative under compression and shear failure, we assume

$$u_{3D}^* = \max(0, u_{3D}(t^*)) \tag{21}$$

The calculation process of 4D-LSM with the multibody failure criterion is illustrated in Fig. 4. The classical stress strength model is

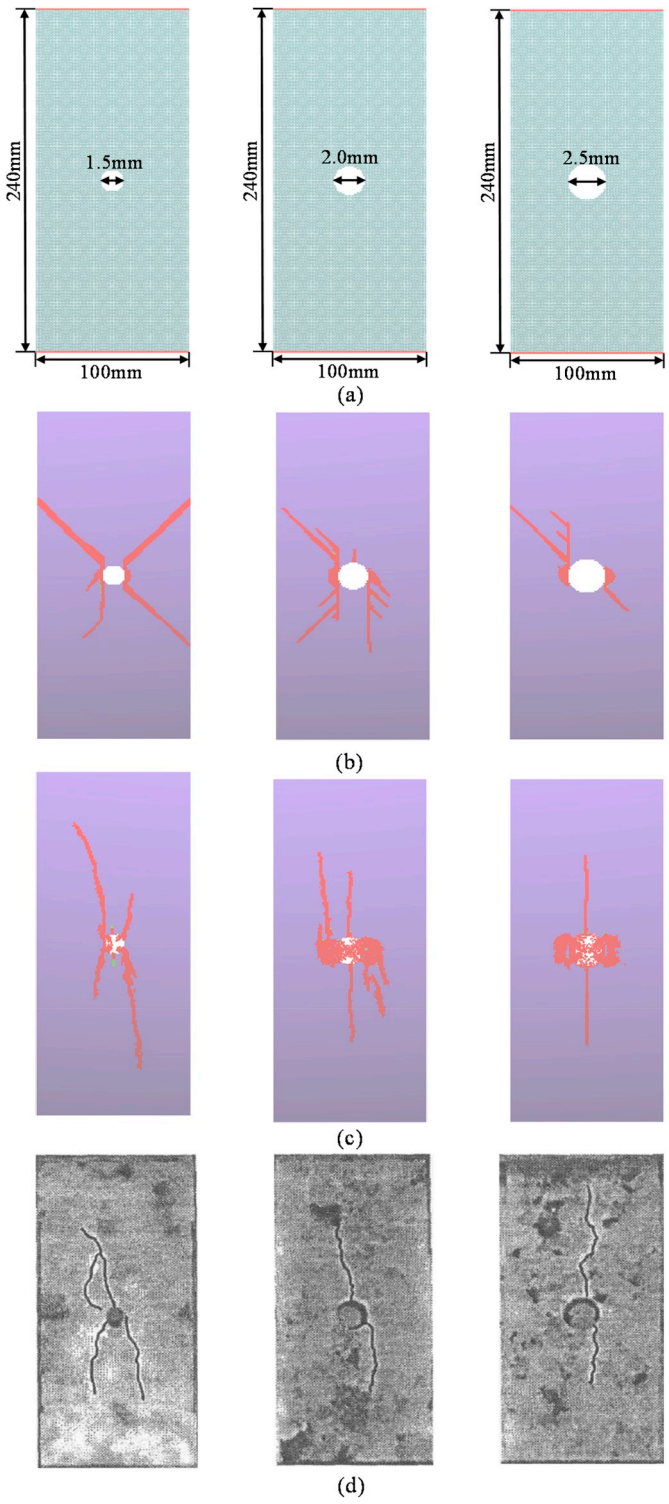

Fig. 8. Failures of specimens that contain a single round hole, as predicted by 4D-LSM. (a) Computational models. (b) Numerical results of 4D−LSM with the original constitutive model. (c) Numerical results of 4D-LSM with the multibody failure criterion. (d) Experimental results from Liang.[29]

embedded in the calculation. The main advantage is that the input parameters are the same as in the continuum-based numerical model, which can be directly determined via conventional rock mechanics tests. However, compared with continuum-based numerical models, the fabric stress tensor calculation involves only deformation of the spring bonds and the classical Cauchy stress tensor and Cauchy strain tensor are not involved; hence, the model is more flexible for solving problems that involve large rigid-body rotations.

3. Verification

3.1. Computational model

A strength model in continuum mechanics describes the mechanical response of a material under uniaxial compression or uniaxial tension tests as a single point. A numerical model should treat the uniaxial tension or compression test as a three-dimensional boundary value problem. The computational model that is used in this section is illustrated in Fig. 5. The specimen is a rectangular column of size 80 mm × 80 mm × 160 mm and the particle diameter is 1.0 mm. The model includes a total of 1.024 million particles. The dimensions of this numerical specimen are comparable to those of specimens in conventional rock or concrete experiments. If the particle diameter is smaller, the failure morphology of the specimen should be more similar to those that are observed in the physical tests. However, due to the limited computational power of our workstations, we can only solve a computational model with limited resolution. The boundary conditions are presented in Fig. 5a. For the uniaxial tension test, the bottom surface of the specimen is fixed and an upward velocity is applied to the top surface; the reaction force $F(t)$ and displacement $u(t)$ of the top surface are recorded during the calculation. Then, the load-displacement curve of the digital specimen can be obtained and the tensile strength σ^t_{4D-LSM} is calculated as

$$\sigma^t_{4D-LSM} = F^*/A \tag{22}$$

where F^* is the maximum loading force and A is the sectional area. For the uniaxial compression problem, the uniaxial compressive strength σ^c_{4D-LSM} can be obtained via a similar method and the only difference is that the direction of the velocity load is opposite in the top surface. In this section, the load velocity is 1 mm/s, which is sufficiently small for eliminating the rate dependence and guaranteeing quasi-static loading. Similar to the model of Kazerani et al.,[27] our model moves only approximately 2 nm in a single calculation step; hence, the whole loading process can be regarded as being in a quasi-static state. The material parameters of the computational model are listed in Table 1. To investigate the influence of the postfailure behavior of the spring bond, the *dRatio* is set to 0.3, 0.5, 0.7, and 0.9.

3.2. Numerical results

The numerical results of the uniaxial compressive and tensile tests are presented in Fig. 5b–d. In Fig. 5b, the tensile strength of the model does not vary dramatically with *dRatio* and remains stable at approximately 8.8 MPa (which is close to the input value that is listed in Table 1). However, according to Fig. 5c, the compressive strength changes with *dRatio*. The compressive strength attains its highest value of 114.93 MPa when *dRatio* = 0.3. Hence, the postfailure behavior of the spring bond influences the uniaxial compressive failure of the specimen. The UCS/T ratio is plotted in Fig. 5d, which decreases rapidly and subsequently increases slightly as *dRatio* increases. When *dRatio* = 0.3, the UCS/T ratio is 13.27, which is the theoretical value that is based on the modified Mohr-Coulomb criterion with these input parameters. Hence, the UCS/T ratio of rock can be reproduced for 4D-LSM by using the multibody strength criterion. The recommended value of *dRatio* in this work is 0.3. Our strategy is to include the UCS/T ratio in 4D-LSM as an input parameter by introducing the multibody failure criterion, which is based on the macroscopic stress-based strength model. For a discontinuum-based model, the distinct feature of the proposed solution is that the input parameters are classical mechanical parameters and no calibration of micromechanical parameters is required. The discreteness of the discontinuum-based model is not violated.

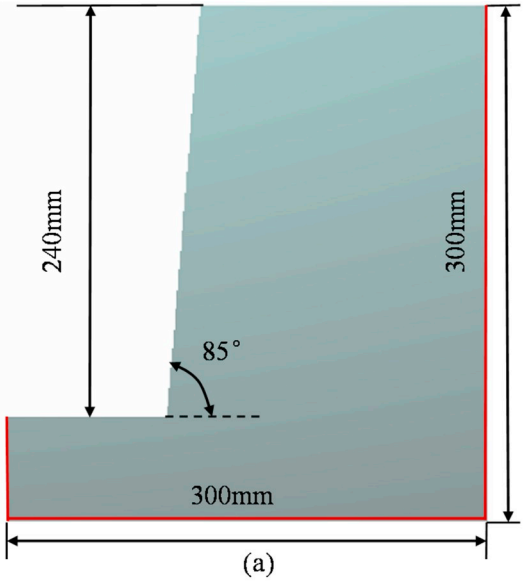

(a)

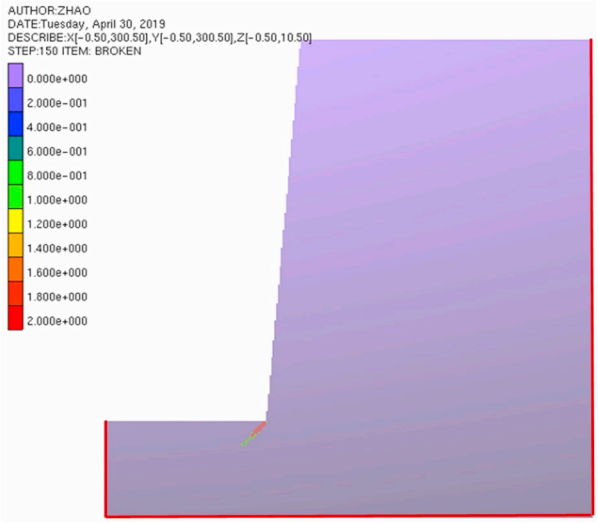

(b)

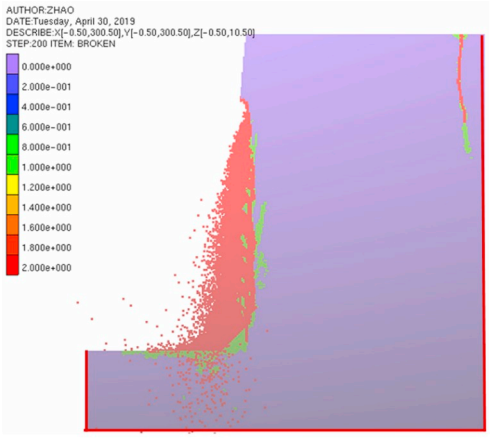

(c)

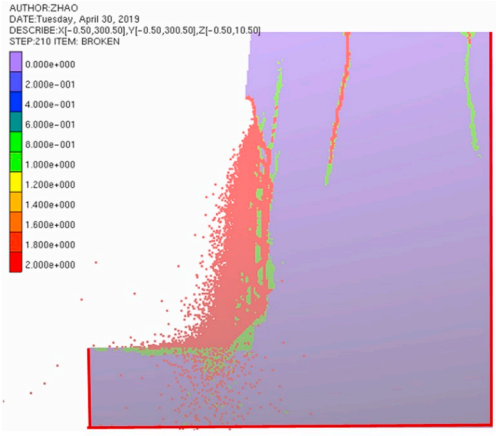

(d)

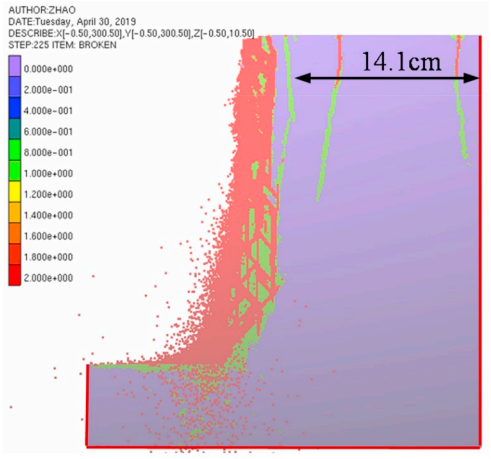

(e)

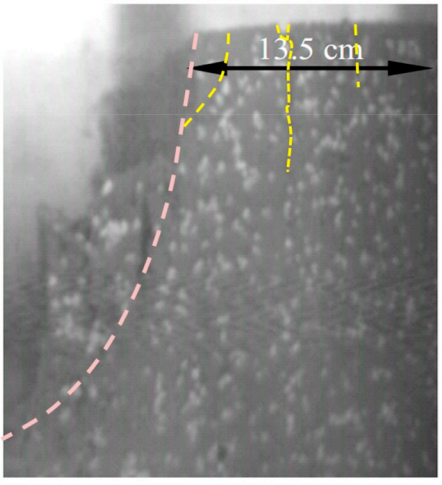

(f)

Fig. 9. Numerical modelling of the progressive failure of a slope under a centrifuge test. (a) Computational model. (b)Failure pattern under gravity acceleration of 30 g. (c) failure pattern under gravity acceleration of 40 g. (d)Failure pattern under gravity acceleration of 42 g. (e)Failure pattern under gravity acceleration of 45. (f) Experimental observed failure pattern under 45 g (from Zhang et al.[30]).

4. Application

4.1. Influence of the porosity on the UCS/T ratio

Computational models with porosities of 5%, 10%, 15%, and 20% are generated by randomly removing a specified number of particles to introduce spatial pores. All the material parameters and boundary conditions are the same as in the previous example. Numerical uniaxial compression and uniaxial tension tests are conducted. The failure results of these models are presented in Fig. 6. With the increase of the porosity, the fracture zone under compression tends to expand, whereas no change in the fracture zone under tension is readily observed. As shown in Fig. 7, both the compressive strength and the tensile strength decrease with the increase of the porosity. However, the porosity and the tensile strength are linearly correlated, whereas a nonlinear and more sensitive relationship is identified between the porosity and the compressive strength (see Fig. 7a). In Fig. 7b, the UCS/T ratio decreases with the increase of the porosity, which is consistent with the experimental observation of Chen et al.[28] This example demonstrates that with the solution that is provided in this work, 4D-LSM can be used as predictive tool to investigate the mechanical responses of porous material (e.g., foam concrete) if the mechanical parameters of the base material (concrete) are known.

4.2. Crack propagation in a square column with a single circular hole

In this section, we establish three square models with circular holes of various diameters. The size of the model is 10 mm × 10 mm × 24 mm, where the diameter d of the circular hole through the model is 1.5 mm, 2.0 mm, and 2.5 mm. The diameter of the particles in the model is 0.1 mm and the total number of particles is approximately 2.4 million. A front view of the model is presented in Fig. 8a. The parameters of the model are obtained from Liang[29] and the loading mode is the same as that of the uniaxial compression test. To evaluate the effect of introducing the multibody failure criterion, 4D-LSM with the original brittle constitutive model is also used to solve the same problem. The corresponding results are presented in Fig. 8b, where the fracture morphologies of the rock specimens differ from the experimental results, especially for the compression-shear failure of rock specimens, which cannot be well reproduced. When the multibody failure criterion is adopted, as shown in Fig. 8c, the crack propagation mode of the model changes substantially with the hole size, which is consistent with the physical experimental results of Liang.[29] According to Fig. 8c, when $d = 1.5$ mm, the crack mainly grows along the diagonal direction of the model and the model mainly presents the mode of shear failure; when $d = 2.0$ mm, both tensile cracks that extend along the direction of the maximum principal stress and shear cracks that develop along the diagonal appear in the model. Finally, the failure of the model presents a shear-splitting composite failure mode. When $d = 2.5$ mm, the cracks in the model mainly propagate along the direction of the maximum principal stress and the model eventually presents a splitting failure mode. Therefore, we conclude that the multibody failure criterion is necessary for 4D-LSM, which not only solved the low UCS/T ratio problem but also enhanced its performance in describing the crack propagation of rock under complex stress conditions.

4.3. Progressive failure of a rock slope

In this section, 4D-LSM is further employed to solve a classical progressive failure problem in geotechnical engineering. Based on the centrifugal test of Zhang et al. on a slope model,[30] a corresponding computational model is established, as illustrated in Fig. 9a. During the centrifugal test, the rock slope is progressively destroyed by increasing the applied gravitational acceleration (the unit is $g = 9.8\ \mathrm{m/s^2}$). The centrifuge tests were simulated by using the gravity increase method. The implementation is straightforward for LSM; additional details can be found in the work of Lian et al.[31] Our numerical simulation results demonstrate that when the gravitational acceleration is 30 g, the fracture zone that is caused by stress concentration appears at the toe of the slope (see Fig. 9b). When 40 g is applied,the first obvious tensile crack begins to appear at the top of the slope, far from the slope surface, due to the influence of tensile stress (see Fig. 9c). When the gravitational acceleration was 42 g, a tensile crack appeared at the slope top and a second tensile crack was readily observed in the middle of the top surface (see Fig. 9d). A third tensile crack appeared at the top of the slope near the slope surface and a sliding fracture zone was formed when the gravitational acceleration was 45 g (see Fig. 9e). The locations of the slide plane and tensile cracks are similar to those in the physical experiment (see Fig. 9f). This example involves the fracturing and failure of rock that will eventually be transformed into granular-like material. However, the performance of 4D-LSM in solving granular flows has not been well investigated. Therefore, the postfailure stage of rock that is transformed into granular-like material remains unknown and future investigation is highly recommended. This whole process involves large rigid-body rotations. Since both the mechanical and failure calculations of 4D-LSM with the multibody failure criterion are free from the influence of the rigid-body rotation, the approach that is developed in this work is robust.

5. Discussion

Reviewing the development history of strength theory of materials,[24] the stress-based strength models have been well verified against many experimental results. For a numerical method, the effective use of existing strength models can enhance its performance in solving various failure problems of these materials, which is one of the major advantages of continuum-based numerical models.[32] The approach that is developed in this work can be regarded as a solution for discontinuum-based models that avoids the low UCS/T problem by utilizing these macroscopic stress-based strength models. It is straightforward to implement other strength models, such as the Hoek–Brown model, which can enable 4D-LSM to handle the failure and fracturing of most board materials.

Cohesive-zone-model-based numerical models[33,34] have been widely used in the analysis of rock failure, in which failure of the cohesive element (interface element) is judged based on the stress state of the adjacent elements. However, these models typically introduce additional stiffness parameters for the pre-failure stage, which might cause instability. The computational costs of these models are typically high, especially in the three-dimensional case. Moreover, the treatment of a large deformation requires special treatment of the rigid-body rotation, which could be a source of accumulative error. In terms of the elastic parameters, 4D-LSM can maintain consistency between the pre-failure and postfailure stages. Moreover, the failure and fracture treatments are straightforward and easy to understand. However, as a newly developed model, 4D-LSM has many shortcomings. This work is a preliminary exploration of 4D-LSM in solving the low UCS/T ratio problem. How to incorporate more complex constitutive mechanical responses, such as viscoelasticity and highly non-linear dynamic deformation responses[35–37] prior to material failure, remains to be determined.

Four-dimensional interaction is a hypothesis in modern physics. The physical experimental results of a quantum effect support the consideration of the 4D topology.[38] Rigid-body rotation is a critical issue for large-deformation problems. For example, the treatment of a multibody shear spring in DLSM, an angular spring in LSM, or an angular potential in MD is complex. Incrementally calculating the shear or angular deformation might be a source of accumulated error. In this respect, 4D-LSM provides an easy solution for the large deformation problem since only central interactions are involved.[18]

6. Conclusions

A feasible solution for 4D-LSM for solving the low UCS/T ratio problem in modeling rock materials is developed. The multibody failure criterion of spring bonds is determined by calculating the fiber stress tensor of particles and by utilizing the classical stress-based strength model. We found that the fiber stress tensor could be used to represent the Cauchy stress tensor of the model. Our numerical results demonstrate that the high UCS/T ratio of rock materials can be successfully reproduced by combining the multibody failure criterion that is based on the modified Mohr-Coulomb strength model with a linear softening model. The multibody failure criterion renders 4D-LSM more flexible in describing rock failure. For example, the relationship between the porosity and the UCS/T ratio that is predicted by 4D-LSM is consistent with the results of physical experiments. We also found that the new model enabled 4D-LSM to more realistically describe the crack propagation of rock under compression and shear conditions and the progressive failure of a rock slope. Nevertheless, rock failure is a process with complex nonlinear responses, such as viscosity, rate dependency, hysteretic characteristics, plastic-elastic coupling, and fatigue damage. These problems will be addressed for 4D-LSM in our future work.

Declaration of competing interest

We wish to confirm that there are no known conflicts of interest associated with this publication and there has been no significant financial support for this work that could have influenced its outcome.

Acknowledgements

This research is financially supported by the National Key R&D Program of China (under # 2018YFC0406804) and National Natural Science Foundation of China (Grant No. 11772221).

References

1 Christensen Richard M. Perspective on materials failure theory and applications. *J Appl Mech*. 2016;83(11), 111001.
2 Potyondy DO. Parallel-bond refinements to match macroproperties of hard rock. Continuum and distinct element modeling in Geomechanics. In: *Proceedings, 2nd Internationl FLAC/DEM Symposium: Itasca International*. 2011, 08-04.
3 Scholtès L, Donzé FV. A DEM model for soft and hard rocks: role of grain interlocking on strength. *J Mech Phys osf Solids*. 2013;61(2):352–369.
4 Cho N, Martin CD, Sego DC. A clumped particle model for rock. *Int J Rock Mech Min Sci*. 2007;44(7):997–1010.
5 Kazerani T, Zhao J. Micromechanical parameters in bonded particle method for modelling of brittle material failure. *Int J Numer Anal Methods Geomech*. 2010;34(18):1877–1895.
6 Zhao GF, Fang J, Sun L, Zhao J. Parallelization of the distinct lattice spring model. *Int J Numer Anal Methods Geomech*. 2013;37(1):51–74.
7 Ding X, Zhang L. Simulation of rock fracturing using particle flow modeling: phase i-model development and calibration. In: *45th US Rock Mechanics/geomechanics Symposium*. American Rock Mechanics Association; 2011.
8 Akram MS, Sharrock GB. Physical and numerical investigation of a cemented granular assembly of steel spheres. *Int J Numer Anal Methods Geomech*. 2010;34(18):1896–1934.
9 Schöpfer MP, Abe S, Childs C, Walsh JJ. The impact of porosity and crack density on the elasticity, strength and friction of cohesive granular materials: insights from DEM modelling. *Int J Rock Mech Min Sci*. 2009;46(2):250–261.
10 Donze FV, Bouchez J, Magnier SA. Modeling fractures in rock blasting. *Int J Rock Mech Min Sci*. 1997;34(8):1153–1163.
11 Shiu WJ, Donzé FV, Daudeville L. Compaction process in concrete during missile impact: a DEM analysis. *Comput Concr*. 2008;5(4):329–342.
12 Kozicki J, Donzé FV. A new open-source software developed for numerical simulations using discrete modeling methods. *Comput Methods Appl Mech Eng*. 2008;197(49):4429–4443.
13 Zhao GF, Yin Q, Russell A, Li Y, Wu W, Li Q. On the linear elastic responses of the 2D bonded discrete element model. *Int J Numer Anal Methods Geomech*. 2019;43(1):166–182.
14 Ding X, Zhang L. A new contact model to improve the simulated ratio of unconfined compressive strength to tensile strength in bonded particle models. *Int J Rock Mech Min Sci*. 2014;69(3):111–119.
15 Fakhimi A. Application of slightly overlapped circular particles assembly in numerical simulation of rocks with high friction angles. *Eng Geol*. 2004;74(1–2):129–138.
16 Wu S, Xu X. A study of three intrinsic problems of the classic discrete element method using flat-joint model. *Rock Mech Rock Eng*. 2016;49(5):1813–1830.
17 Zhao GF, Fang J, Zhao J. A 3D distinct lattice spring model for elasticity and dynamic failure. *Int J Numer Anal Methods Geomech*. 2011;35(8):859–885.
18 Zhao GF. Developing a four-dimensional lattice spring model for mechanical responses of solids. *Comput Methods Appl Mech Eng*. 2017;315:881–895.
19 Zhang Z, Yao Y, Mao X. Modeling wave propagation induced fracture in rock with correlated lattice bond cell. *Int J Rock Mech Min Sci*. 2015;78:262–270.
20 Pan Z, Ma R, Wang D, Chen A. A review of lattice type model in fracture mechanics: theory, applications, and perspectives. *Eng Fract Mech*. 2018;190(1):382–409.
21 Jiang C, Zhao GF, Khalili N. On crack propagation in brittle material using the distinct lattice spring model. *Int J Solids Struct*. 2017;118:41–57.
22 Zhao GF, Xia K. A study of mode-I self-similar dynamic crack propagation using a lattice spring model. *Comput Geotech*. 2018;96:215–225.
23 Zhao GF. *Development of Micro-macro Continuum-Discontinuum Coupled Numerical Method*. PhD thesis. Switzerland: EPFL; 2010.
24 Yu MH. Advances in strength theories for materials under complex stress state in the 20th Century. *Adv Mech*. 2004;34(4):529–560.
25 Hondros G. The evaluation of Poisson's ratio and the modulus of materials of a low tensile resistance by the Brazilian (indirect tensile) test with particular reference to concrete. *Aust J Appl Sci*. 1959;10:243–268.
26 Wang Q, Ma G, Wang XJ. Numerical simulation on tensile failure of rock-like heterogeneous material using a modified SPH method. *Int J Comput Methods*. 2015;12(06), 1550039.
27 Kazerani T, Yang ZY, Zhao J. A discrete element model for predicting shear strength and degradation of rock joint by using compressive and tensile test data. *Rock Mech Rock Eng*. 2012;45(5):695–709.
28 Chen X, Wu S, Zhou J. Influence of porosity on compressive and tensile strength of cement mortar. *Constr Build Mater*. 2013;40:869–874.
29 Liang ZZ. *Three-dimensional Failure Process Analysis of Rock and Associated Numerical Tests*. PhD thesis. Shenyang: Northeastern University; 2005.
30 Zhang G, Wang AX, Mu TP, Zhang JM. Study of stress and displacement fields in centrifuge modeling of slope progressive failure. *Rock Soil Mech*. 2008;29(10):2637–2641.
31 Lian JJ, Li Q, Deng XF, Zhao GF, Chen ZY. A numerical study on toppling failure of a jointed rock slope by using the distinct lattice spring model. *Rock Mech Rock Eng*. 2018;51(2):513–530.
32 Liao ZY, Zhu JB, Tang CA. Numerical investigation of rock tensile strength determined by direct tension, Brazilian and three-point bending tests. *Int J Rock Mech Min Sci*. 2019;115:21–32.
33 Jiao YY, Zhang HQ, Zhang XL, et al. A two-dimensional coupled hydromechanical discontinuum model for simulating rock hydraulic fracturing. *Int J Numer Anal Methods Geomech*. 2015;39(5):457–481.
34 Wu Z, Fan L, Liu Q, Ma GW. Micro-mechanical modeling of the macro-mechanical response and fracture behavior of rock using the numerical manifold method. *Eng Geol*. 2017;225:49–60.
35 Li X, Zhang QB, He L, Zhao J. Particle-based numerical manifold method to model dynamic fracture process in rock blasting. *Int J Geomech*. 2016;17(5). E4016014.
36 Li JC, Rong LF, Li HB, Hong SN. An SHPB test study on stress wave energy attenuation in jointed rock masses. *Rock Mech Rock Eng*. 2019;52(2):403–420.
37 Jiang MJ, Yu HS, Harris D. Bond rolling resistance and its effect on yielding of bonded granulates by DEM analyses. *Int J Numer Anal Methods Geomech*. 2006;30(8):723–761.
38 Zilberberg O, Huang S, Guglielmon J, et al. Photonic topological boundary pumping as a probe of 4D quantum Hall physics. *Nature*. 2018;553(7686):59.